

Intermediate magnetic phase of the magnetoelectric compound (Ca,Sr)BaCo₄O₇ described with the superspace formalism

J. Lohr¹, A. L. Larralde², J. Curiale^{3,4}, R. Sánchez^{3,4}, J. Campo⁵, G. J. Cuello⁶,
D. Sheptyakov⁷, L. Keller⁷, M. Kenzelmann⁷, and G. Aurelio^{8,*}

¹Comisión Nacional de Energía Atómica–Laboratorio Argentino de Haces de Neutrones, Centro Atómico Bariloche,
Av. Bustillo 9500 R8402AGP, S. C. de Bariloche, Argentina

²Laboratorio de Cristalografía Aplicada, Escuela de Ciencia y Tecnología, Universidad Nacional de San Martín,
Martín de Irigoyen 3100, Campus Miguelete, San Martín (1650), Buenos Aires, Argentina

³Instituto de Nanociencia y Nanotecnología CNEA-CONICET, Centro Atómico Bariloche,
Av. Bustillo 9500 R8402AGP, S. C. de Bariloche, Argentina

⁴Instituto Balseiro, Universidad Nacional de Cuyo - Comisión Nacional de Energía Atómica,
Av. Bustillo 9500 R8402AGP, S. C. de Bariloche, Argentina

⁵Instituto de Ciencia de Materiales de Aragón (CSIC - Universidad de Zaragoza) and Departamento de Física de Materia Condensada,
Universidad de Zaragoza. C/Pedro Cerbuna 12, E-50009 Zaragoza, Spain

⁶Institut Laue Langevin. 71, Av des Martyrs, BP 156 F-38042 Grenoble, France

⁷Laboratory for Neutron Scattering and Imaging, Paul Scherrer Institut, CH-5232 Villigen PSI, Switzerland

⁸Comisión Nacional de Energía Atómica and CONICET Laboratorio Argentino de Haces de Neutrones. Centro Atómico Bariloche, Av.
Bustillo 9500 R8402AGP, S. C. de Bariloche, Argentina



(Received 22 July 2020; accepted 14 September 2020; published 6 October 2020)

In this work we report the temperature and doping-level evolution of the crystallographic and magnetic properties of the Sr-doped cobaltates Ca_{1-x}Sr_xBaCo₄O₇. The noncollinear ferrimagnetic phase known for the magnetoelectric parent compound is found to persist only for a small amount of Sr doping ($x = 0.02$) and is accompanied by a strong unit cell distortion. In turn, further Sr doping blurs this distortion of lattice parameters and favors other magnetic arrangements. In particular, this work focuses on an intermediate temperature region $62\text{ K} < T < 82\text{ K}$ that shows a *plateau* in the magnetization. Using neutron powder diffraction at selected temperatures and compositions, we have solved the magnetic structure of this intermediate phase. By means of the superspace group theory and its implementation in the Rietveld refinement, we found that the phase belongs to the superspace group $Pna2_1(1/2, 1/2, g)qq0s$ with a basic orthorhombic structure and a modulation of the magnetic moments along the c axis. The propagation vector is $\mathbf{k} = (\frac{1}{2}, \frac{1}{2}, g)$ with $g \sim 0.02$ and possibly dependent on temperature. A modulated spin structure with distinct behaviors of the triangular and kagome cobalt sites is reported in “114” cobaltates.

DOI: [10.1103/PhysRevB.102.134406](https://doi.org/10.1103/PhysRevB.102.134406)

I. INTRODUCTION

The so-called “114” cobaltates $R\text{BaCo}_4\text{O}_7$ were first reported in 2002 for $R=Y$ (Ref. [1]) and, since then, synthesized with other lanthanides. This compound gained attention immediately because, among other properties related to oxygen absorption, it offers the possibility to study frustrated magnetism in the unique topology of a three-dimensional framework of interconnected triangular and kagome layers of Co atoms in a tetrahedral environment. This sublattice of Co atoms that combines triangular-based exchange topology with antiferromagnetic spin interactions causes a strong geometrical frustration, a topic related to intensively studied phenomena in spin ices and multiferroic materials [2,3]. In 2009, Caignaert *et al.* [4] synthesized the $R=\text{Ca}$ member, which then triggered even more exciting features by the mod-

ification of the valence ratio, the crystal symmetry, the charge order, and, most interestingly, the magnetic and electric properties. Contrary to its Ln^{3+} relatives, $\text{CaBaCo}_4\text{O}_7$ develops a ferrimagnetic order below 60 K with a complex noncollinear arrangement of spins [5,6], and it concomitantly displays a dramatic increase of electric polarization of $17\,000\ \mu\text{C}/\text{cm}^2$, driven by exchange striction [7]. Whereas it was initially thought that the compound was ferroelectric [8], it is rather defined as a ferrimagnetic pyroelectric, as the polarization cannot be switched by an external electric field [7,9]. With these findings, the “Ca-114” cobaltate turned a good candidate to study new magnetoelectric and multiferroic materials of spin origin. Some studies have been published since then on the effect of doping the “Ca-114” cobaltate at different sites, and it was proposed that doped systems exhibit complex phase diagrams involving strong competition between ferrimagnetic (FiM) and antiferromagnetic (AFM) order [10,11]. However, the only compounds studied to date with neutron diffraction are the parent compound $\text{CaBaCo}_4\text{O}_7$, a Zn-for-Co substituted

*gaurelio@cab.cnea.gov.ar, she/her/hers

sample $\text{CaBaCo}_{3.97}\text{Zn}_{0.03}\text{O}_7$ (Ref. [12]), and the Ni-for-Co $\text{CaBaCo}_{3.9}\text{Ni}_{0.1}\text{O}_7$ [13]. The closely-related “114” ferrite has also been reported to show quite interesting features, as well as the Fe-doped $\text{CaBaCo}_{4-x}\text{Fe}_x\text{O}_7$ [14,15].

The substitution of Ca with Sr, which in oxides such as manganites and cobaltates usually gives rise to novel properties enhanced by disorder and size effects [16,17], has not been explored so far using neutron techniques. Recently, we reported on the synthesis and room temperature structure of Sr-doped $\text{CaBaCo}_4\text{O}_7$ and showed that small amounts of Sr at the Ca site can induce changes in the macroscopic magnetization [18]. We also reported that the solubility limit is below 10% Sr. In this work, we focus on the crystallographic and magnetic order at selected temperatures for a series of samples with varying Sr doping below the solubility limit. To this end, we have combined neutron powder diffraction (NPD) data collected at different sources and instruments, together with macroscopic properties measurements. The superspace group formalism [19–21] is used in this work to analyze the NPD, which allows for the complete determination of the global symmetry of the system (both of the magnetic and nuclear contributions) expressed with crystallographic rules. We will discuss the phases that form in the temperature region where the magnetization presents a *plateau* which in many aspects connects with all other members of the RBaCo_4O_7 family and the different substitutions previously proposed in the literature, pointing to the central role of distortions and symmetry.

II. EXPERIMENTAL METHODS

A. Synthesis

Polycrystalline samples of nominal $\text{CaBaCo}_4\text{O}_7$ (hereafter called Sr0) and $\text{Ca}_{1-x}\text{Sr}_x\text{BaCo}_4\text{O}_7$ with $x = 0.02$ (Sr2), $x = 0.05$ (Sr5), and $x = 0.07$ (Sr7) were prepared by conventional solid-state reaction. High-purity powders of previously dried CaCO_3 , BaCO_3 , SrCO_3 , and Co_3O_4 were thoroughly mixed in an agate mortar at stoichiometric weights. After a de-carbonation process at 1173 K for 12 h, the mixtures were pressed into pellets. Pellets were annealed during 12 h to 15 h at 1373 K and cooled at 3 K/min in the furnace. After a regrinding the compression and annealing at 1373 K in air were repeated, and as a final step samples were quenched from 1373 K to liquid nitrogen to obtain the stoichiometric compound.

B. Neutron powder diffraction

High-resolution NPD experiments were performed at the Institut Laue-Langevin (ILL) in France and at the Paul Scherrer Institute (PSI) in Switzerland. NPD data from ILL were collected using the D2B high-resolution diffractometer for samples Sr2 and Sr5 [22], covering an angular detector span of 150° with a step of 0.05° . The collimated beam on the sample was of $32\text{ mm} \times 12\text{ mm}$ using 250 mm horizontal slits. A NaCaAlF standard was used to calibrate the neutron's wavelength, yielding $\lambda = (1.5943 \pm 0.0001)\text{ \AA}$. Measurements were performed in vanadium cylinders of 6 mm diameter and 8 cm height filled with sample, at room temperature and se-

lected temperatures between 10 K and 120 K, using a displex device with an average collection time of 4 h.

A thermodiffraction experiment was performed in the high-intensity two-axes diffractometer D20 also at ILL for the Sr2 sample [22] in the range $20\text{ K} \leq T \leq 200\text{ K}$. Data were collected on warming with programmed ramps of 1 K/min and diffractograms saved every 2 min. Sample holders were identical to those used in the D2B experiment. Silicon and NaCaAlF standards were used to calibrate the wavelength, yielding $\lambda = (1.3582 \pm 0.0002)\text{ \AA}$.

NPD data with a longer wavelength and lower background were collected at the DMC cold neutron diffractometer [23] of PSI for a second batch of the Sr5 sample, with $\lambda = 2.4584\text{ \AA}$. Finally, for the Sr7 sample the HRPT high-resolution diffractometer [24] at PSI was used to study selected temperatures ranging from 1.5 K to 350 K using various wavelengths, namely, $\lambda = 1.4940\text{ \AA}$, $\lambda = 1.8858\text{ \AA}$, and $\lambda = 2.4480\text{ \AA}$.

All data were analyzed with the FULLPROF suite [25]. Thermodiffraction data were plotted using the LAMP software [26]. For the Rietveld refinement of the crystal structure and the magnetic order, different approaches were used that are detailed in the Results. The tools we used include FULLPROF [25], ISODISTORT [27,28], and several utilities within the Bilbao Crystallographic Server [29–31].

C. Magnetic properties

DC magnetization measurements were performed using two SQUID magnetometers and a PPMS in VSM mode at low temperature ($5\text{ K} < T < 350\text{ K}$) under various applied magnetic fields between 1 kOe and 140 kOe, at warming/cooling rates of 2 K/min. Magnetization vs T data were collected on cooling and warming under an applied magnetic field of 5 kOe (labeled FCC and FCW, respectively) or cooled in zero-field conditions and measured on subsequent warming (labeled ZFC). Magnetization was also measured at constant temperatures as a function of applied field between -140 kOe and 140 kOe in a PPMS. The ac susceptibility as well as the specific heat were measured using two PPMS, at ICMA and PSI. The ac-susceptibility was measured with frequencies ranging from 1 Hz to 1 kHz under $H_{\text{ac}} = 10\text{ Oe}$ and $H_{\text{dc}} = 0\text{ Oe}$. For all these experiments, small fragments of the sintered ceramic pellets were used.

III. RESULTS

A. Temperature evolution of macroscopic magnetization

As mentioned above, we showed in Ref. [18] that low levels of Sr-for-Ca substitution in $\text{CaBaCo}_4\text{O}_7$ affect the magnetic properties quite dramatically, as evidenced in dc- and ac-susceptibility measurements. By increasing the fraction of Sr at the Ca site from 0 to 10%, the net magnetization at low temperature drops from almost $1\text{ }\mu_{\text{B}}/\text{f.u.}$ to less than $0.01\text{ }\mu_{\text{B}}/\text{f.u.}$ Moreover, two additional features are revealed by Sr substitution: a magnetization *plateau* below $\sim 80\text{ K}$ and an apparent additional transition showing hysteresis between warming and cooling below 60 K. These features are shown in Fig. 1 where we present the magnetization (M) of the samples in the temperature range $5\text{ K} < T < 200\text{ K}$ under an applied magnetic field (H) of 5 kOe, for each value of Sr substitution.

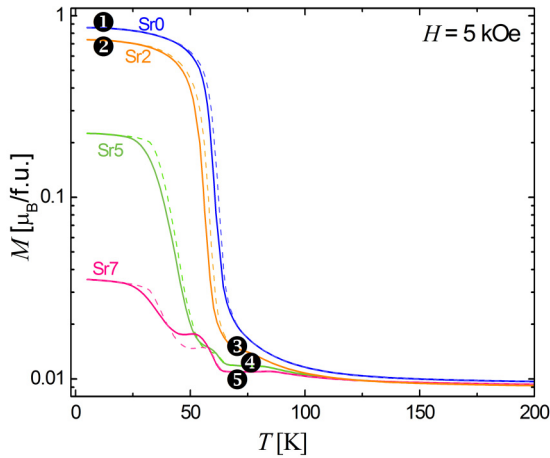


FIG. 1. Magnetization as a function of temperature under an applied field of 5 kOe for $\text{Ca}_{1-x}\text{Sr}_x\text{BaCo}_4\text{O}_7$ with $x = 0, 0.02, 0.05$, and 0.07 . Solid lines represent data collected on cooling, whereas dashed lines correspond to data collected on warming. The numbered circles indicate selected temperatures that are explored using NPD in the present work.

In all cases there is an increase in the net magnetization with decreasing temperature, but only Sr2 is most similar to the parent compound. For the Sr2 sample, the T_C looks shifted a few degrees—to 53 K—similar to what has been observed in the Zn-substituted compound [12]. For higher doping, the net increase of the magnetization is much lower (note the logarithmic scale in Fig. 1). We have indicated within numbered circles certain selected temperatures, which will be explored using NPD in the present work.

In these compounds the ac susceptibility is highly sensitive to the presence of new magnetic interactions introduced by doping and/or nonstoichiometry oxygen [12,32]. In Fig. 2(a) we show the $\chi'(T)$ curves collected at different frequencies for the Sr5 sample. Similar measurements for Sr0 and Sr2 were reported in Ref. [18]. We observe that the addition of more Sr produces at least three evident effects: (i) It reduces dramatically the net magnetization that the samples reach at low temperature, (ii) it enhances a transition located around 80 K, which relates to the magnetization plateau [shown in Fig. 2(b) for reference], and (iii) it reveals another transition at ≈ 35 K. We do not detect a frequency dependence of the peaks positions in the ac susceptibility characteristic of spin-glass or cluster-glass phases [33]. Finally, panels (c) and (d) in Fig. 2 show the specific heat curve and its derivative with respect to temperature, respectively, for sample Sr7. The two dips in the derivative match perfectly with the temperature limits of the magnetization plateau (colored area) and suggest a sequence of magnetic phase transitions. To explore this plateau, we measured the magnetization curves as a function of the applied magnetic field close to 70 K, for all our samples, which are presented in Fig. 3. All of them, still far from the theoretical saturation value, behave in a similar manner showing a slight decrease of the magnetization as the Sr concentration increases. A linear regime is observed below magnetic fields of ~ 5 T and ~ 9 T for Sr0 and Sr7, respectively. In this regime, it is expected that the multidomain magnetic structure in the

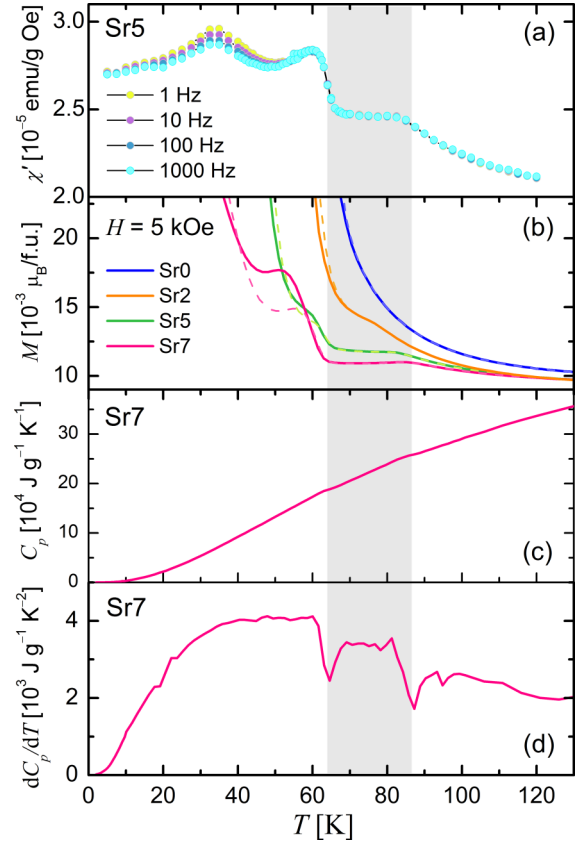


FIG. 2. (a) Temperature dependence of the real part of the ac susceptibility under an applied field $H_{ac} = 10$ Oe and $H_{dc} = 0$ Oe for $\text{Ca}_{0.95}\text{Sr}_{0.05}\text{BaCo}_4\text{O}_7$ ($x = 0.05$) measured at different frequencies. (b) Zoomed region of the magnetization curves measured under a field of 5 kOe. (c)–(d) Specific heat and its derivative with respect to temperature for a sample with $x = 0.07$. The shadowed area corresponds to the region we refer to as the magnetization plateau.

powder microcrystals evolves to a single domain for each microcrystal. The deviation from a linear regime at high fields suggests that the magnetic order may be quite complex, as we will show in the following sections.

B. Temperature evolution of crystal structure

The effect of the Sr-for-Ca substitution on the crystal structure is very small at room temperature [18]. On the contrary, the magnetic properties are strongly affected by substitution, so it is interesting to analyze the structure as a function of Sr substitution at lower temperatures, where magnetic interactions become stronger. The room-temperature space group of $\text{CaBaCo}_4\text{O}_7$ is #33 as labeled in the International Tables of Crystallography [34]. In this work we have chosen to describe it using the standard setting $\text{Pna}2_1$ [35].

Room temperature refinements for samples Sr2 and Sr5 were reported by us in Ref. [18]. Sample Sr7 was measured at a later stage at the HRPT diffractometer in PSI, using two wavelengths. The room temperature structure obtained from the joint Rietveld refinement of both datasets is summarized in Table I and the refinement is shown in Fig. 4. Except for weak reflections originating from the steel body of a thermocouple (second row of ticks), no additional reflections are observed,

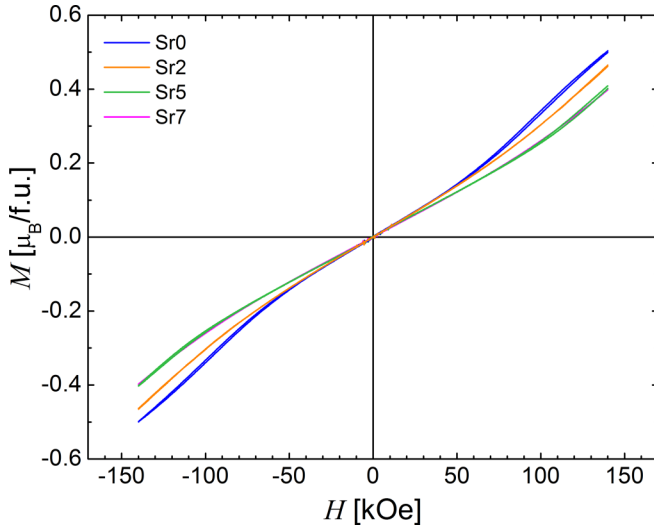


FIG. 3. Magnetization as a function of the applied magnetic field at 75 K for $\text{Ca}_{1-x}\text{Sr}_x\text{BaCo}_4\text{O}_7$ with $x = 0, 0.02, 0.05$ and at 70 K for $x = 0.07$.

which agrees with our XRD measurements done to carefully check for Sr segregation (not shown). The structural model obtained in the refinement is in perfect agreement with that reported for the parent compound [4] in the $Pbn2_1$ setting. The equivalence between both models was checked using the utility for comparing structures in the Bilbao Crystallographic Server [29].

It is interesting to note that, in the most general case, the “114”-cobaltate crystal structure derives from a high-

TABLE I. Structural parameters for $\text{Ca}_{0.93}\text{Sr}_{0.07}\text{BaCo}_4\text{O}_7$ at 300 K. Data collected in the HRPT diffractometer at PSI using $\lambda_1 = 1.4940$ Å and $\lambda_2 = 1.8858$ Å. Fractional coordinates correspond to the space group $Pna2_1$ with all atoms in the Wyckoff position 4a. The z coordinate of the Ba atom at $z = 0.5$ was fixed as a reference value following Ref. [4].

| Atom | x | y | z | B_{iso} [Å ²] |
|----------------------|------------|----------------------|------------|------------------------------------|
| Ca/Sr | 0.6714(6) | 0.0015(11) | 0.1266(6) | 0.84(6) |
| Ba | 0.6655(5) | 0.0027(7) | 0.5000 | 0.82(6) |
| Co1 | 0.0000(15) | 0.001(2) | 0.0591(10) | 0.9(1) |
| Co2 | 0.1739(9) | -0.001(2) | 0.3111(13) | 1.0(1) |
| Co3 | 0.0868(8) | 0.2504(19) | 0.8112(11) | 0.9(1) |
| Co4 | 0.9179(8) | 0.2648(18) | 0.3198(11) | 0.9(1) |
| O1 | 0.0004(6) | -0.0063(17) | 0.7484(7) | 0.79(6) |
| O2 | 0.4932(5) | 0.0016(11) | 0.7704(6) | 1.03(6) |
| O3 | 0.2599(6) | 0.7850(12) | 0.2204(9) | 1.7(1) |
| O4 | 0.7440(5) | 0.7326(10) | 0.7866(8) | 1.3(1) |
| O5 | 0.1536(4) | -0.0562(7) | 0.4996(8) | 1.53(7) |
| O6 | 0.1043(3) | 0.2088(7) | 0.9995(10) | 1.45(7) |
| O7 | 0.9452(3) | 0.2598(7) | 0.5020(11) | 1.41(6) |
| a [Å] | 11.0166(1) | | | |
| b [Å] | 6.29047(7) | | | |
| c [Å] | 10.1938(1) | | | |
| $\chi^2_{\lambda_1}$ | 1.48 | $\chi^2_{\lambda_2}$ | 1.61 | |
| $R_{B_{\lambda_1}}$ | 3.66 | $R_{B_{\lambda_2}}$ | 4.64 | |

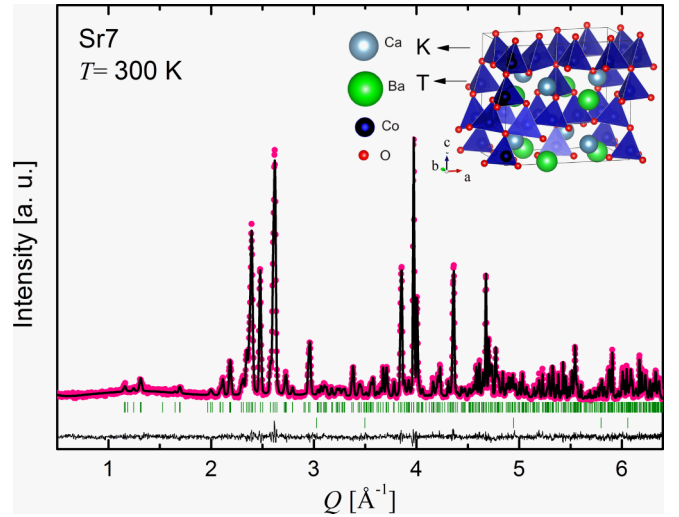


FIG. 4. Rietveld refinement for sample Sr7 from NPD data collected at room temperature in the high-resolution diffractometer HRPT at PSI (results only shown for $\lambda = 1.89$ Å). Vertical bars at the bottom indicate Bragg reflections from the orthorhombic $Pna2_1$ phase and from a cubic phase for the furnace thermocouple. The solid line at the bottom represents the difference between the experimental and calculated patterns. The inset shows the position of the Co-O tetrahedra in the unit cell as well as the Ca and Ba layers. The kagome (K) and triangular (T) layers of tetrahedra are also indicated.

symmetry hexagonal phase belonging to space group $P6_3mc$ (# 186) as observed in the original Swedenborgite [36] that gives its name to this structural family. Different distortions give rise to a number of lower-symmetry structures. These can be caused by doping with other elements, by applying pressure, or by a change in temperature. Distortions help lift the geometric frustration of the kagome and triangular layers, and in some cases even allow for a net magnetic moment, as in $\text{CaBaCo}_4\text{O}_7$. For instance, the closely-related YBaCo_4O_7 cobaltate nicely illustrates this [37–39]. It undergoes a sequence of transitions when temperature is decreased from room temperature: $P31c \rightarrow Pna2_1 \rightarrow P2_1$ which are all isotropy subgroups of the higher-symmetry $P6_3mc$, although the latter has not been observed experimentally at least in oxygen-stoichiometric samples. The $P31c \rightarrow Pna2_1$ is a first-order transition induced by temperature, and it involves complex displacements of the oxygen atoms that can be pictured as rotations of the CoO_4 tetrahedra around the c axis in both the kagome and triangular sublattices [40]. It has been shown that this is an efficient way to adjust the bond valence requirements of Ba^{2+} which is strongly underbonded in this family of compounds [4,38,41] and is the driving force for the successive phase transitions. In the case of the “Ca-114” compound discussed in this work, the highest-symmetry hexagonal $P6_3mc$ phase is not realized, however the trigonal subgroup $P31c$ has been only observed above 1073 K [42]. By replacing the Ln^{3+} by Ca^{2+} the orthorhombic $Pna2_1$ symmetry is favored. The buckling of the CoO_4 tetrahedra is much stronger compared with its Ln^{3+} relatives and the structure displays the largest orthorhombic distortion with respect to the parent hexagonal phase, so the “Ca-114” member effectively removes frustration.

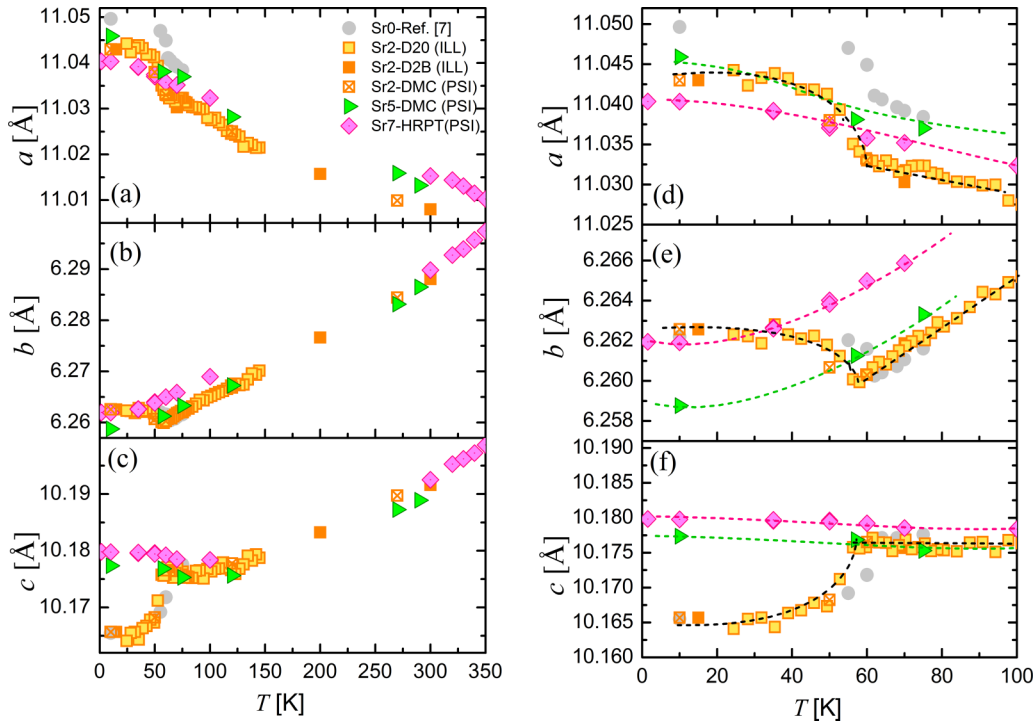


FIG. 5. Thermal evolution of the lattice parameters with respect to an orthorhombic cell, between 1.5 K and 350 K (a)–(c), for samples with increasing Sr substitution ($0 \leq x \leq 0.07$) collected at different NPD instruments. Data from Ref. [7] are included as a reference for the parent compound. The panel in the right (d)–(f) shows a zoomed region at low temperature. The dashed lines are only guides to the eye.

In Fig. 5 we show the evolution of lattice parameters with temperature for all the studied samples. The space group and crystallographic structure have shown to remain the same in the paramagnetic range from 120 K up to 350 K (left panel). In the figure we have also included the data reported by Caignaert *et al.* [7] from NPD, as a reference for the parent compound. Our own Sr0 reference sample was measured at 15 K for comparison, being in excellent agreement with Ref. [7]. Moving to Sr substitution, we observe that the Sr2 sample shows the same temperature dependence of lattice constants as the parent compound, with a strong lattice distortion around T_C . Let us recall that lattice axes are related to meaningful properties of the crystal: The a direction corresponds to the net magnetic moment (easy axis) in the parent compound, and the c direction is the normal to the cobalt kagome and triangular layers and corresponds to the polar axis, i.e., the electric polarization direction. Abrupt variations in each of these cell parameters are directly related to these properties.

Further Sr substitution reveals that the low-temperature behavior of lattice parameters, enlarged in the right panel of Fig. 5, changes substantially with respect to the low-Sr compositions, which is consistent with the changes in the magnetism of the system. The abrupt distortion around the T_C vanishes, the a parameter is monotonically decreasing with increasing temperature, as the parent compound at higher temperatures, while the b parameter shows a smooth positive expansion with increasing temperature. The c parameter is slightly decreasing with T below 80 K and for higher temperatures it increases as in the parent compound. These results highlight the strong magnetoelastic coupling of the FiM phase reported in Ref. [7] and turn the lattice param-

eters behavior into an additional fingerprint for this particular magnetic arrangement. It should be remarked that the accurate determination of the lattice parameters at low temperature is of fundamental importance for the analysis of the magnetic propagation vectors that will be discussed in the following sections. The overall behavior summarized in Fig. 5 will be used as a reference for such analyses.

C. Magnetic diffraction

One of our main motivations to perform neutron diffraction at different temperatures was to correlate the various features observed in the magnetization curves with the magnetic phases of the samples, focusing on the spots indicated with numbers in Fig. 1. To this end, we first measured our reference sample, Sr0, at 15 K ① to check the magnetic model for the FiM phase and start from a solid basis. The refinement is shown in Fig. 6(a). Next we explored samples with increasing Sr content: Sr2, Sr5, and Sr7. The diffractogram at 15 K for sample Sr2 ② collected at D2B is presented in Fig. 6(b). The magnetic contribution in both cases was successfully refined using the same FiM model proposed by Caignaert *et al.*, [5] corresponding to a propagation vector $\mathbf{k} = (0, 0, 0)$ with respect to the orthorhombic cell and represented by the magnetic space group $Pna'2'_1$ (#33.147). It corresponds to the 1D-irreducible representation (IR) $m\text{GM}3$ —following the notation of the Bilbao Crystallographic Server—which allows for a ferromagnetic component along the a axis. This is consistent with the macroscopic magnetization of samples Sr2 and Sr0 showing a similar trend with only a slight decrease in the net magnetization at low temperature (① and ② in Fig. 1). All magnetic reflections have a resolution-limited

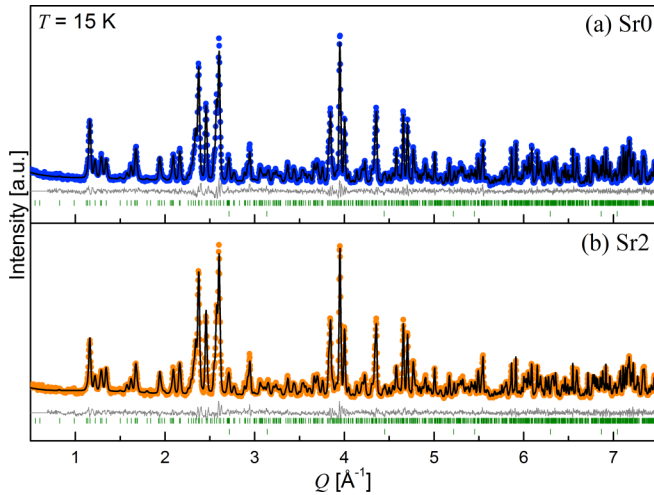


FIG. 6. Rietveld refinement for samples $\text{CaBaCo}_4\text{O}_7$ (Sr0) and $\text{Ca}_{0.98}\text{Sr}_{0.02}\text{BaCo}_4\text{O}_7$ (Sr2) from NPD data collected at 15 K in the high-resolution diffractometer D2B at ILL ($\lambda = 1.5943$ Å). Vertical bars at the bottom (first row) indicate nuclear and magnetic reflections from the space group $Pn2_1'$ (#33.147), whereas the second row indicates the reflections coming from the Al cryostat. The solid line at the bottom represents the difference between the experimental and calculated patterns.

width, indicating that a full 3D, long-range order is achieved. No additional features are observed in the D2B diffractogram of the Sr2 sample, although very low intensity peaks are present in measurements performed at DMC (PSI), that will be discussed in a separate work.

When temperature is increased, however, the diffractogram of the Sr2 sample departs from that of the parent compound. According to the latter, the FiM phase should disappear at 60 K and the sample should become paramagnetic, showing only nuclear diffraction. We followed the evolution of the magnetic reflections with increasing temperature for Sr2, between 20 K and 200 K at the high-flux D20 diffractometer (ILL) using a wavelength $\lambda = 1.3582$ Å. Results are shown in Fig. 7. It is important to remark that the quality of these data only allow for a qualitative description, as the counting time is short (2 min) and the background is quite high, so only the most intense magnetic peaks are well resolved. Nonetheless, we do observe that the magnetic reflections corresponding to the FiM model discussed above (marked with arrows in Fig. 7) indeed vanish close to 60 K, in particular the intense magnetic reflection at $Q = 1.18$ Å⁻¹. But in the approximate interval 50 K < T < 80 K, a different kind of magnetic scenario is suggested by a new peak centered around $Q \approx 1.37$ Å⁻¹ (marked with an asterisk in Fig. 7) as well as a contribution from diffuse magnetic scattering, typical of short-range order. It is not until above 80 K that the diffractograms show only nuclear reflections, and still then there remains an increased background of diffuse scattering around $Q \approx 1.4$ Å⁻¹ indicating that short-range magnetic correlations persist; in fact even the diffraction pattern at room temperature from the Sr7 sample presented in Fig. 4 shows this feature. This diffuse scattering is closely related to magnetic correlations when the system is close to the 2D spin structure of staggered chirality, namely the $\sqrt{3} \times \sqrt{3}$ phase (in terms of the underlying

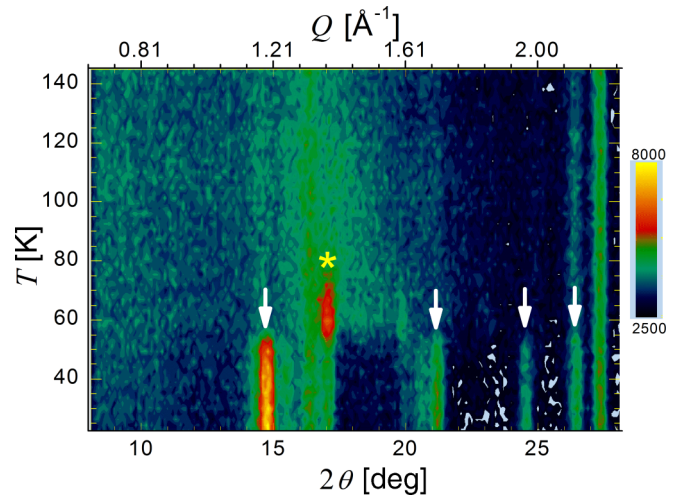


FIG. 7. Thermodiffraction data for sample Sr2 ($\text{Ca}_{0.98}\text{Sr}_{0.02}\text{BaCo}_4\text{O}_7$) collected at D20 (ILL) using $\lambda = 1.3582$ Å. The figure shows the T projection along 2θ (bottom axis) and Q (top axis) for the region of interest. White arrows denote the main magnetic reflections of the FiM phase, whereas the asterisk denotes the main reflection of the intermediate phase.

hexagonal parent structure). Actually, the value of $Q \approx 1.4$ Å⁻¹ corresponds to a (200) reflection for the a value of ~ 6.3 Å in the hexagonal setting. An interesting discussion on this topic can be found in Ref. [43].

In contrast with the FiM phase, the observed intermediate magnetic phase between 50 K < T < 80 K is not accounted for by a propagation vector $\mathbf{k} = (0, 0, 0)$ and is more likely to come from an AFM arrangement, that makes sense with the *plateau* observed in the magnetization curves which—let us recall—is only slightly evident for the Sr2 sample and much more pronounced for Sr7. To analyze this intermediate magnetic phase between 60 and 80 K, we measured sample Sr2 at 70 K at D2B. We also measured sample Sr5 at 75 K at the DMC cold-neutron diffractometer of PSI and sample Sr7 at 70 K at HRPT using two different wavelengths. The diffractograms obtained are plotted in Fig. 8 and correlate to points ③, ④, and ⑤ in Fig. 1. For the three datasets, the analysis of the magnetic order started by searching for the magnetic propagation vector \mathbf{k} . The magnetic contribution in the 70–80 K range shows only a few peaks above the background in sample Sr2 from data collected at D2B, but is better resolved in data from PSI for Sr5 and Sr7. The commensurate propagation vector that comes closest to account for the magnetic peaks is $\mathbf{k} = (\frac{1}{2}, \frac{1}{2}, 0)$. However, the refinements carried out using models derived from this hypothesis were not completely satisfactory for Sr2 and Sr7, and definitely incorrect for Sr5, which was measured at a slightly higher temperature. Such approximate model is nonetheless a possible phase for this compound, and we will recall it for the analysis of the lower temperature region in a separate work. For the Sr5 sample at 75 K the propagation vector $\mathbf{k} = (\frac{1}{2}, \frac{1}{2}, 0)$ does not account for the magnetic reflections properly; in particular for the double-peak around $Q = 1.35$ Å⁻¹. The propagation vector for Sr5 turned out to be incommensurate with the crystal lattice, with a value $\mathbf{k} = (\frac{1}{2}, \frac{1}{2}, 0.024)$. The possibility of an

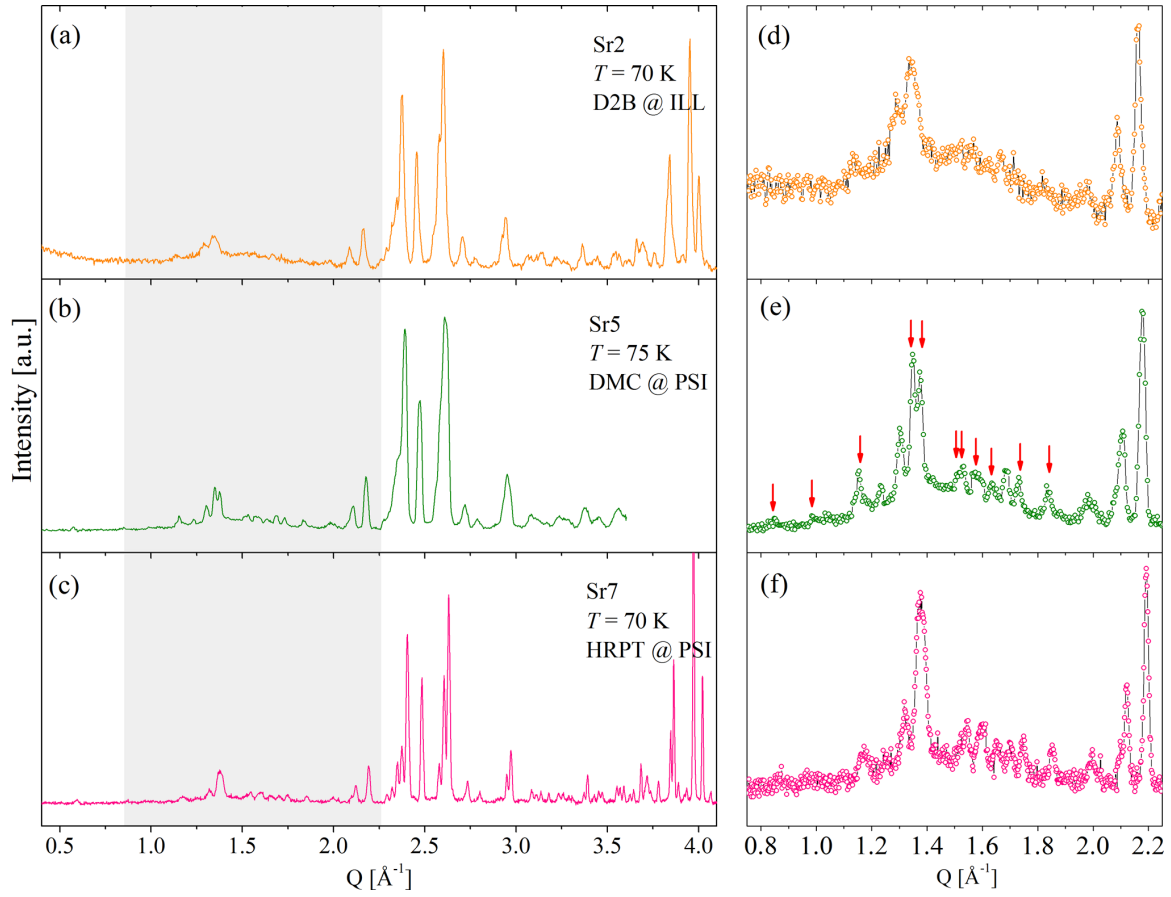


FIG. 8. Diffraction patterns collected for samples (a) Sr2 at 70 K, data from D2B (ILL), (b) Sr5 at 75 K, data from DMC (PSI), and (c) Sr7 at 70 K from HRPT (PSI). A low- Q region showing the most intense magnetic peaks [marked with arrows in panel (e)] is presented in the right panel for each sample (d)–(f).

incommensurate intermediate phase had been mentioned in Ref. [12] when discussing the Zn-for-Co substitution but not explored in depth.

In order to refine our data with an incommensurate magnetic model, we use the superspace groups approach [19], a comprehensive and robust method to study incommensurate modulated structures both for aperiodic crystals and magnetic ordering [20]. In the superspace formalism a magnetic structure is described by a basic structure, related to the nuclear paramagnetic cell, in addition to a series of magnetic modulation functions with propagation vector \mathbf{k} that describe the variation from the basic structure of the magnetic moments [20]. The basic structure is described by a conventional magnetic space group and is at the same time related to the paramagnetic nuclear space group. An additional internal coordinate x_4 is defined such that the modulated magnetization, in the presence of a single propagation vector, can be expressed in a Fourier series as:

$$\mathbf{M}_j(x_4) = \mathbf{M}_{j,0} + \sum_{n=1}^{\infty} [\mathbf{M}_{j,ns} \sin(2\pi n x_4) + \mathbf{M}_{j,nc} \cos(2\pi n x_4)], \quad (1)$$

where j runs along the magnetic sites of the asymmetric unit in the basic structure and n corresponds to the

harmonics of k . We truncate the sum at $n = 1$ because we do not observe higher order satellites in the NPD experiment. Then Eq. (1) reads $\mathbf{M}_j(x_4) = \mathbf{M}_{j,0} + \mathbf{M}_{j,s} \sin(2\pi x_4) + \mathbf{M}_{j,c} \cos(2\pi x_4)$. The superspace is $(3 + 1)$ -dimensional and the fourth dimension refers to the internal coordinate $x_4 = \mathbf{k} \cdot \mathbf{r}_{lj}$ where \mathbf{r}_{lj} represents the position of atom j in the l th unit cell (with l a lattice translation of the basic structure). The modulation waves $\mathbf{M}_{j,c} \cos(2\pi x_4)$ and $\mathbf{M}_{j,s} \sin(2\pi x_4)$ must comply with the symmetry constraints imposed by the magnetic superspace group (MSSG). This formalism has been very recently implemented in FULLPROF [21] in combination with the ISOTROPY suite [27] to allow for the refinement of neutron diffraction data.

The combination between the paramagnetic $Pna2_11'$ and the propagation vector $\mathbf{k} = (\frac{1}{2}, \frac{1}{2}, g)$ with $g \sim 0.02$ leads to four possible MSSG that are described by the IRs labeled mQ1QA1, mQ2QA2, mQ3QA3, and mQ4QA4 [27]. The refinement was attempted in all possible MSSG but a good solution was found only in the case of mQ3QA3 which corresponds to the MSSG $Pna2_11'(1/2, 1/2, g)qq0s$ with its origin at $(0, \frac{1}{2}, 0, 0)$ with respect to the paramagnetic structure. The term $\mathbf{M}_{j,0}$ is null because of symmetry, so that this magnetic structure is not compatible with a net magnetic moment. There are in this example no relations imposed by symmetry on the modulated waves for Co atoms sitting at $4a$ sites ($\mathbf{M}_{j,s}$ and $\mathbf{M}_{j,c}$). However, for the final refinements, the magnetic mo-

TABLE II. Structural and magnetic parameters for $\text{Ca}_{0.93}\text{Sr}_{0.07}\text{BaCo}_4\text{O}_7$ at 70 K. Data collected in the HRPT diffractometer at PSI using $\lambda_1 = 2.4480 \text{ \AA}$ and $\lambda_2 = 1.8858 \text{ \AA}$. Fractional coordinates correspond to the superspace group $Pna2_11'(1/2, 1/2, g)qq0s$ with its origin at $(0, \frac{1}{2}, 0, 0)$.

| Atom | x | y | z | $B_{\text{iso}} [\text{\AA}^2]$ | | | |
|--------------------------------------------------------------|---------------------------------------|--------------|-------------|---------------------------------|----------|------------|--|
| Ca1 | 0.67175(43) | 0.00531(79) | 0.12788(49) | 0.49(6) | | | |
| Sr1 | 0.67175(43) | 0.00531(79) | 0.12788(49) | 0.49(6) | | | |
| Ba1 | 0.66545(33) | 0.00389(51) | 0.50000 | 0.37(6) | | | |
| Co1 | −0.0013(11) | 0.0081(16) | 0.05754(88) | 0.9(1) | | | |
| Co2 | 0.17166(80) | −0.0021(16) | 0.31229(96) | 0.9(1) | | | |
| Co3 | 0.08655(63) | 0.2448(16) | 0.81012(81) | 0.4(1) | | | |
| Co4 | 0.91762(65) | 0.2694(14) | 0.31946(86) | 0.7(1) | | | |
| O1 | 0.00023(53) | −0.0108(13) | 0.74766(56) | 0.67(6) | | | |
| O2 | 0.49251(37) | −0.00110(90) | 0.77010(51) | 0.47(6) | | | |
| O3 | 0.26092(44) | 0.78721(96) | 0.21846(72) | 0.88(9) | | | |
| O4 | 0.74336(42) | 0.73044(80) | 0.79159(67) | 0.64(8) | | | |
| O5 | 0.15218(29) | −0.05736(47) | 0.49912(55) | 0.69(6) | | | |
| O6 | 0.10899(25) | 0.20580(48) | 0.99824(74) | 0.66(6) | | | |
| O7 | 0.94791(25) | 0.26358(53) | 0.50407(84) | 0.70(5) | | | |
| Modulated magnetic moment parameters and standard deviations | | | | | | | |
| Atom | $ \mathbf{M}_c $ | ϕ_c | θ_c | $ \mathbf{M}_s $ | ϕ_s | θ_s | |
| Co1 | 2.4(1) | 174(3) | 90 | 1.3(2) | −90 | 90 | |
| Co2/3/4 | 1.91(3) | −37(2) | 90 | | | | |
| $a [\text{\AA}]$ | 11.03519(3) | | | | | | |
| $b [\text{\AA}]$ | 6.26586(4) | | | | | | |
| $c [\text{\AA}]$ | 10.17849 (3) | | | | | | |
| k | $\frac{1}{2}, \frac{1}{2}, 0.0197(2)$ | | | | | | |
| $\chi^2_{\lambda_1}$ | 1.48 | | | $\chi^2_{\lambda_2}$ | 2.16 | | |
| $R_{B_{\lambda_1}}$ | 3.38 | | | $R_{B_{\lambda_2}}$ | 3.43 | | |
| $R_{\text{mag}_{\lambda_1}}$ | 14.6 | | | $R_{\text{mag}_{\lambda_2}}$ | 16 | | |

ments were constrained to lay on the a - b plane, in accordance with the Sr0 ferrimagnetic phase and other magnetic models reported for similar compounds of the “114” Swedenborgite family [37,38]. As we used spherical coordinates for the analysis, this means that the polar angles θ_c and θ_s were forced to 90° . As the refinement proceeded, further constraints were introduced in the Fourier amplitudes. We found that the $\mathbf{M}_{j,s}$ for the Co moments at the kagome sites had negligible values, so we set $|\mathbf{M}_{j,s}| = 0$ for j running in sites Co2, Co3, and Co4. This results in magnetic moments that are only modulated in their moduli, but their direction does not change with the internal coordinate x_4 . For the Co laying in the triangular layer, Co1, we obtained the best refinement for a modulation of the \mathbf{M}_s term with ϕ_s fixed at -90° . Finally, as we arrived at very similar values for the three independent kagome Co sites, we constrained them to have the same \mathbf{M}_c . This is a reasonable assumption given their crystallographic similarity and considering the fact that the statistics of the available NPD data does allow enough precision to refine them individually. Note, however, that they are not constrained by symmetry to be identical. To sum up, the complete magnetic model was refined using five parameters, which are listed in Table II. In Fig. 9 we present the results for the joint refinement of data collected at HRPT in PSI for $\lambda_1 = 2.45 \text{ \AA}$ and $\lambda_2 = 1.89 \text{ \AA}$ for sample Sr7. The structural and magnetic parameters for the obtained model are listed in Table II together with the factors for goodness of fits.

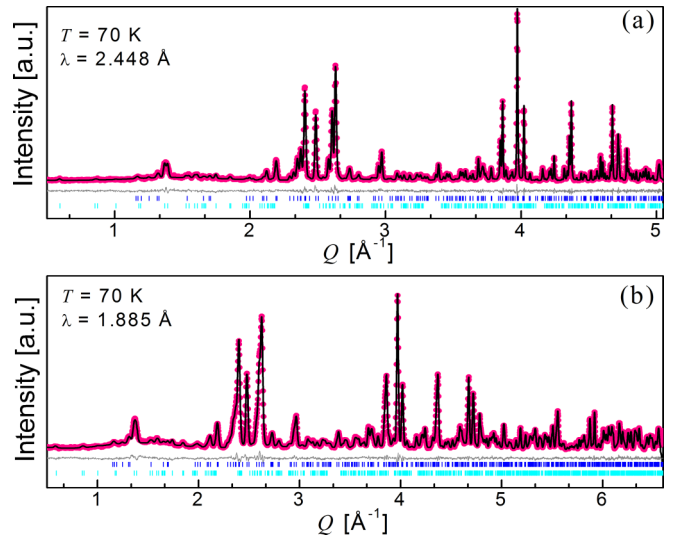


FIG. 9. Rietveld refinement for sample $\text{Ca}_{0.93}\text{Sr}_{0.07}\text{BaCo}_4\text{O}_7$ (Sr7) from NPD data collected at 70 K in the high-resolution diffractometer HRPT at PSI for two wavelengths: $\lambda_1 = 2.4480 \text{ \AA}$ (a) and $\lambda_2 = 1.8858 \text{ \AA}$ (b). The refinement was performed jointly (multipattern refinement). Vertical bars at the bottom indicate Bragg reflections from nuclear and magnetic contributions in different colors. The solid line at the bottom represents the difference between the experimental and calculated patterns. The model corresponds to the MSSG $Pna2_11'(1/2, 1/2, g)qq0s$.

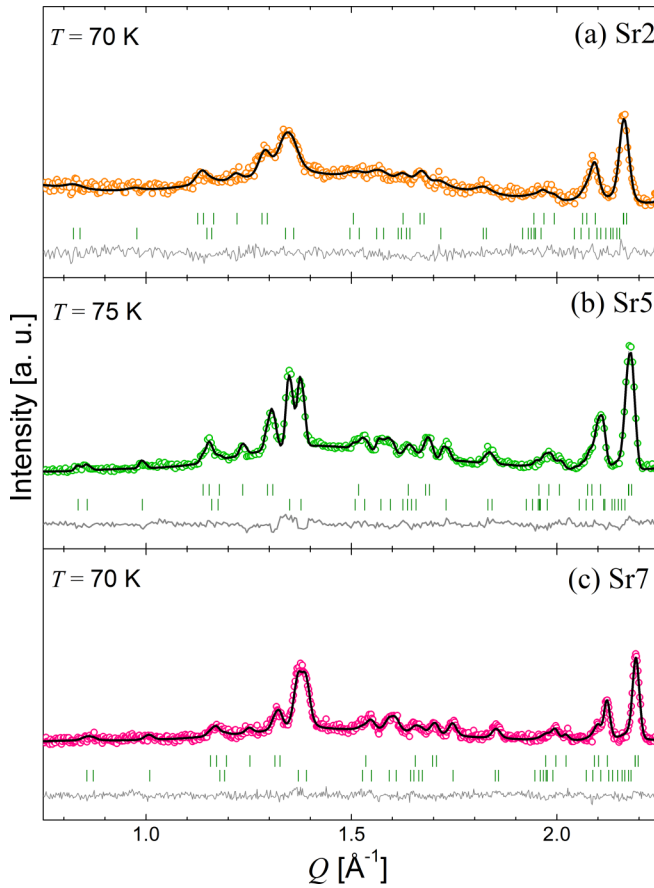


FIG. 10. Low- Q region of the Rietveld refinements for samples Sr2 (a), Sr5 (b), and Sr7 (c) at 70 K, 75 K, and 70 K, respectively. Data were collected at D2B (ILL), DMC (PSI), and HRPT (PSI) for each sample. The first row of vertical bars at the bottom indicates Bragg reflections from the nuclear phase and the second corresponds to magnetic reflections, both accounted for by the superspace group $Pna2_11'(1/2, 1/2, g)qq0s$ as explained in the text. The line at the bottom represents the difference between the experimental and calculated patterns.

Next we refined the data for sample Sr5 collected at DMC with cold neutrons of $\lambda = 2.46$ Å. In this case, the shorter Q range in the diffractogram does not allow for a refinement of all the nuclear structural parameters as well as the magnetic, so we kept the former fixed using the atomic positions of the Sr7 sample. The magnetic model obtained was practically the same as for Sr7. For Sr2, measured at D2B (ILL) with $\lambda = 1.59$ Å, we again refined both the nuclear and magnetic parameters. For samples Sr7 and Sr5 the background was modeled with Chebyshev polynomials of degree 15 to 18. For the Sr2 sample this method did not account satisfactorily for the region of diffuse scattering, so the background was refined by interpolation of selected points. The resulting magnetic model for all the refinements is the same, so considering that all datasets were from different samples at different instruments, the model seems quite robust. A magnified low- Q region of the three refinements is shown in Fig. 10. The higher temperature at which data were collected for Sr5 suggests there may develop a gradual evolution of the modulation vector with temperature, i.e., $g = g(T)$. For Sr2 and Sr7, the

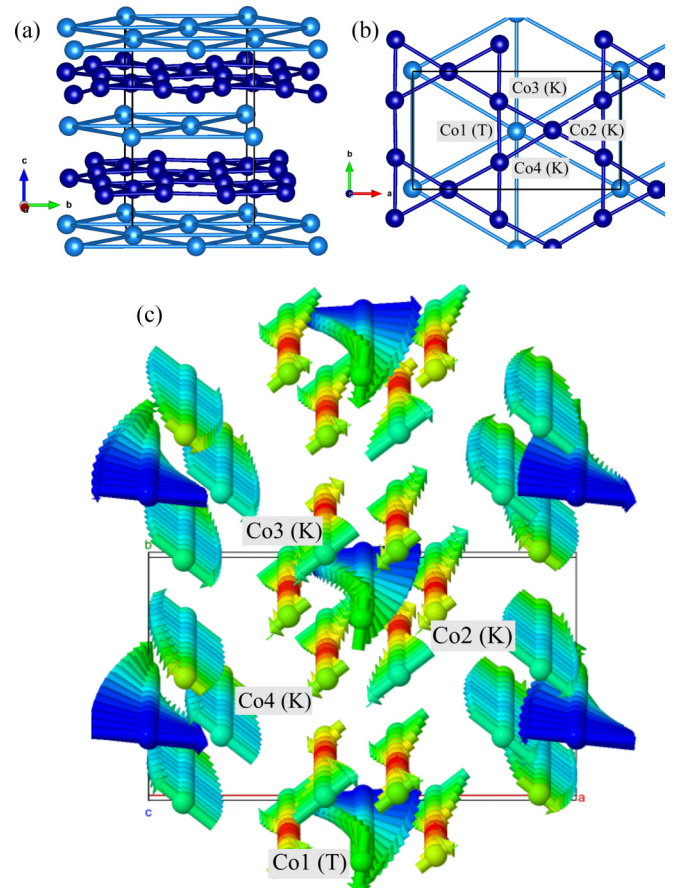


FIG. 11. (a),(b) Views along the a and c axes of the cobalt network in the structure of $\text{Ca}_{1-x}\text{Sr}_x\text{BaCo}_4\text{O}_7$ showing the kagome and triangular layers in different colors. (c) 3D view along c of the first 14 cells of the incommensurate modulated magnetic phase of $\text{Ca}_{1-x}\text{Sr}_x\text{BaCo}_4\text{O}_7$ between 60 K and 80 K. Graphic produced with JSmol [44]. The color scheme is based on vector moduli, ranging from red (min) to blue (max).

refined values of g are slightly smaller, so the peaks that are split around $Q \sim 1.35 - 1.4$ Å⁻¹ in the Sr5 sample partially overlap in the case of Sr2 and Sr7. At 70 K we observe still two distinct reflections, though quite overlapped, whose width is well accounted for by the instrumental resolution without any additional contribution.

Eventually, at lower temperatures the propagation vector locks in to a commensurate periodicity with $\mathbf{k} = (\frac{1}{2}, \frac{1}{2}, 0)$. But also with cooling, new things start to happen in the diffractograms—as anticipated by the magnetization curves—falling already outside the region we defined as the *plateau*. It seems natural that the magnetic model must then change to allow for a weak FM component. However, this analysis is beyond the scope of the present paper and will be presented separately.

The magnetic model proposed in this work for the intermediate phase in the $62 \text{ K} < T < 82 \text{ K}$ temperature region is sketched in Fig. 11. Panels (a) and (b) show the cobalt network in the unit cell, highlighting with different colors the triangular and kagome layers in perspective (a) and projected along the c axis (b). Panel (c) shows a supercell of size $a \times 2b \times 14c$ that corresponds approximately to 1/4 of the

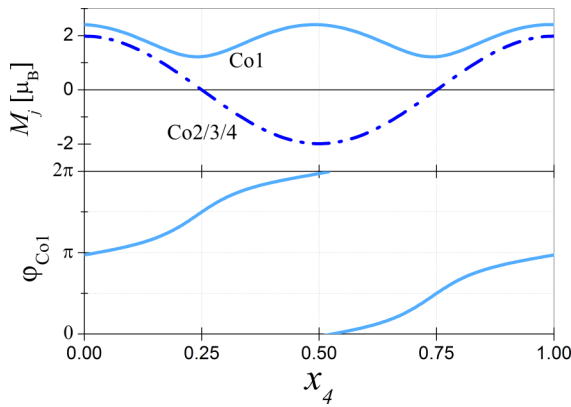


FIG. 12. (Top) Representation of the magnetic moments of Co atoms in the triangular layer Co1 (light blue) and Co2 atoms in the kagome layer (dark blue) along the fourth axis of the $(3 + 1)$ -D space, calculated from the refined parameters at 70 K in sample Sr7. (Bottom) Variation of the azimuthal angle of Co1 represented between 0 and 2π .

modulation along c (around 55 cells). The color scheme is based on the vector moduli. To illustrate how the different Co sites behave along the internal coordinate x_4 —the fourth axis of the $(3 + 1)$ -D space—we present in Fig. 12 the modulated magnetic moments for Co1 and Co2 (similar to Co3 and Co4) and the azimuthal angle ϕ for Co1. These were calculated using Eq. (1) to obtain the module and direction of \mathbf{M}_j using the parameters refined for sample Sr7 at 70 K.

IV. DISCUSSION

In this paper we report the incommensurate magnetic phase that occurs in the Sr-substituted magnetoelectric compound $\text{CaBaCo}_4\text{O}_7$ in the intermediate temperature range $62 \text{ K} < T < 82 \text{ K}$. The parent compound exhibits a complex non-collinear ferrimagnetic order below 60 K. However, even a very small degree of replacement of Sr for Ca in the structure result in the stabilization of an AFM order in a narrow temperature range around 70 K. Evidence of this intermediate phase can be found in several previous studies, sometimes as a subtle variation of slope in the inverse susceptibility or magnetization, or as an unexplained feature in the ac susceptibility [10,33,45,46]. In Ref. [12] NPD data registered as a function of temperature in a Zn-for-Co substituted sample ($\text{CaBaCo}_{3.97}\text{Zn}_{0.03}\text{O}_7$) clearly showed that a different, possibly incommensurate phase is present between 54 K and 77 K but the authors did not solve the magnetic structure. However, we believe that the model described here can account for the data they present for 68 K.

The complex magnetic order we have found in this work using NPD corresponds to zero applied field and can account for the deviation from linearity of the magnetization as a function of magnetic field we showed in Fig. 3. As we are measuring powder samples, the directions of propagation of the modulated structure are randomly oriented under an applied magnetic field, and as this field is increased they may rotate, reorient, and deform all of which may result in an increase in magnetization. It is expected that interesting additional features arise in the magnetic order under intense magnetic fields that would deserve a separate study of single crystals.

We have used the superspace formalism to propose a model for the intermediate magnetic structure of doped-“Ca-114” cobaltates. This approach represents a very powerful tool and allows for the description of the spins modulation in terms of the symmetry and crystallographic description. Our model shows that at this intermediate temperature, the Co spins sitting at triangular layers follow a different modulation than those located at kagome sites. The former present a helical rotation along the c axis together with a modulation of their moduli, whereas the Kagome spins only show a modulation in their moduli. The modulation along c has a periodicity of around 55 unit cells, and our data suggest that this period is a function of temperature. Below 60 K, the propagation vector locks in to the value $\mathbf{k} = (\frac{1}{2}, \frac{1}{2}, 0)$, as we will show in more detail in a future work. This hypothesis would also explain the 55 K data in Ref. [12] for $\text{CaBaCo}_{3.97}\text{Zn}_{0.03}\text{O}_7$. To the best of our knowledge, a modulation of the spins in Swedenborgites perpendicular to the kagome layers has only been reported for $\text{CaBa}(\text{Co}_3\text{Fe})\text{O}_7$ [47]. Such structures can have interesting implications on the multiferroic properties of this family of compounds.

V. CONCLUSIONS

To sum up, in this paper we have followed the evolution of the structural and magnetic phases of Sr-doped $\text{CaBaCo}_4\text{O}_7$ from 10 K to 350 K, as a function of temperature and Sr doping. Due to the large amount of information revealed by NPD and macroscopic measurements, we focused the discussion specially on the AFM intermediate phase that manifests in the magnetization, specific heat, and ac susceptibility. The phase belongs to the superspace group $Pna2_1(1/2, 1/2, g)qq0s$ with a basic orthorhombic structure and a modulation of the magnetic moments along the c axis. A model for this phase is proposed, although it is interesting to note that a similar phenomenology has already been observed for other substitutions to the parent compound. These similarities highlight the strong competition of interactions and the potential role of small distortions to modify the phase diagram and bring about the diversity of interesting phenomena in this class of materials.

ACKNOWLEDGMENTS

This work is part of a research project supported by AN-PCyT (Argentina) under Grant No. PICT-2017-0725, and by CONICET under Grant PIP 490 /2012, Universidad Nacional de Cuyo under Grant No. SECTyP UNCuyo 06/C592, Laboratorio Argentino de Haces de Neutrones and Min-CyT. J.C. would like to acknowledge the use of Servicio General de Apoyo a la Investigación-SAI, Universidad de Zaragoza and support from grants PGC-2018-099024-B-I00-ChiMag from the Ministerio de Ciencia e Innovación de España and i-COOPB20319 from CSIC. Additional support from Diputación General de Aragón (DGA-M4) is also acknowledged. This work is partly based on experiments performed at the Swiss spallation neutron source SINQ, Paul Scherrer Institute, Villigen, Switzerland. We also acknowledge ILL and their staff for the beamtime allocation and technical assistance. G.A. and M.K. acknowledge

the Swiss Leading House for the Latin American region for a Seed Money Grant. G.A. is deeply grateful to the IUPAP for a travel grant for Woman in Science that allowed her to attend the superb 2019 Erice School on Magnetic

Crystallography, which made a big part of this work possible. Valuable discussions with Juan Rodríguez Carvajal and Oscar Fabelo on the use of MSSG in Fullprof are greatly appreciated.

- [1] M. Valldor, *Solid State Sci.* **4**, 923 (2002).
- [2] A. P. Ramirez, *Annu. Rev. Mater. Sci.* **24**, 453 (1994).
- [3] C. Lacroix, P. Mendels, and F. Mila, *Introduction to Frustrated Magnetism: Materials, Experiments, Theory*, Vol. 164 (Springer, New York, 2011).
- [4] V. Caignaert, V. Pralong, A. Maignan, and B. Raveau, *Solid State Commun.* **149**, 453 (2009).
- [5] V. Caignaert, V. Pralong, V. Hardy, Ch. Ritter, and B. Raveau, *Phys. Rev. B* **81**, 094417 (2010).
- [6] Z. Qu, L. Ling, L. Zhang, L. Pi, and Y. Zhang, *Solid State Commun.* **151**, 917 (2011).
- [7] V. Caignaert, A. Maignan, K. Singh, Ch. Simon, V. Pralong, B. Raveau, J. F. Mitchell, H. Zheng, A. Huq, and L. C. Chapon, *Phys. Rev. B* **88**, 174403 (2013).
- [8] K. Singh, V. Caignaert, L. C. Chapon, V. Pralong, B. Raveau, and A. Maignan, *Phys. Rev. B* **86**, 024410 (2012).
- [9] R. D. Johnson, K. Cao, F. Giustino, and P. G. Radaelli, *Phys. Rev. B* **90**, 045129 (2014).
- [10] T. Sarkar, M. Motin Seikh, V. Pralong, V. Caignaert, and B. Raveau, *Appl. Phys. Lett.* **100**, 232401 (2012).
- [11] M. Seikh, T. Sarkar, V. Pralong, V. Caignaert, and B. Raveau, *Phys. Rev. B* **86**, 184403 (2012).
- [12] M. M. Seikh, V. Caignaert, E. Suard, K. P. Meher, A. Maignan, and B. Raveau, *J. Appl. Phys.* **116**, 244106 (2014).
- [13] C. Dhanasekhar, A. K. Das, R. Singh, A. Das, G. Giovannetti, D. Khomskii, and A. Venimadhav, *Phys. Rev. B* **96**, 134413 (2017).
- [14] M. M. Seikh, A. K. Kundu, V. Caignaert, and B. Raveau, *J. Alloys Compd.* **656**, 166 (2016).
- [15] D. Turkin, G. Bazuev, and A. Korolev, *J. Magn. Magn. Mater.* **422**, 66 (2017).
- [16] G. Aurelio, J. Curiale, R. D. Sánchez, and G. J. Cuello, *J. Phys.: Condens. Matter* **21**, 326002 (2009).
- [17] G. Aurelio, R. D. Sánchez, J. Curiale, and G. J. Cuello, *J. Phys.: Condens. Matter* **22**, 486001 (2010).
- [18] G. Aurelio, J. Curiale, F. Bardelli, R. Junqueira Prado, L. Hennet, G. Cuello, J. Campo, and D. Thiaudiere, *J. Appl. Phys.* **118**, 134101 (2015).
- [19] A. Janner and T. Janssen, *Acta Crystallographica Section A* **36**, 399 (1980).
- [20] J. M. Perez-Mato, J. L. Ribeiro, V. Petricek, and M. I. Aroyo, *J. Phys.: Condens. Matter* **24**, 163201 (2012).
- [21] J. Rodríguez-Carvajal and J. Villain, *C. R. Phys.* **20**, 770 (2019).
- [22] G. J. Cuello, G. Aurelio, F. Bardelli, and F. Cantargi, Structure and magnetism in the frustrated cobalt compound (Y,Ni)BaCo₄O_{7+d}, Institut Laue-Langevin (ILL) (2013), doi: 10.5291/ILL-DATA.5-24-530.
- [23] J. Schefer, P. Fischer, H. Heer, A. Isacson, M. Koch, and R. Thut, Nuclear Instruments and Methods in Physics Research Section A: Accelerators, Spectrometers, Detectors and Associated Equipment **288**, 477 (1990).
- [24] P. Fischer, G. Frey, M. Koch, M. Könnicke, V. Pomjakushin, J. Schefer, R. Thut, N. Schlumpf, R. Bürge, U. Greuter *et al.*, *Phys. B: Condens. Matter* **276**, 146 (2000).
- [25] J. Rodríguez-Carvajal, *Abstracts of the Satellite Meeting on Powder Diffraction of the XV Congress of the IUCr, Toulouse, France* (1990), p. 127.
- [26] LAMP, the Large Array Manipulation Program, http://www.ill.eu/data_treat/lamp/the-lamp-book/.
- [27] H. T. Stokes, D. Hatch, and B. Campbell, ISOTROPY Software Suite, iso.byu.edu (2017).
- [28] H. T. Stokes, D. M. Hatch, B. J. Campbell, and D. E. Tanner, *J. Appl. Crystallogr.* **39**, 607 (2006).
- [29] M. I. Aroyo, J. Perez-Mato, D. Orobengoa, E. Tasci, G. de la Flor, and A. Kirov, *Bulg. Chem. Commun* **43**, 183 (2011).
- [30] M. I. Aroyo, J. M. Perez-Mato, C. Capillas, E. Kroumova, S. Ivantchev, G. Madariaga, A. Kirov, and H. Wondratschek, *Zeitschrift für Kristallographie-Crystalline Materials* **221**, 15 (2006).
- [31] M. I. Aroyo, A. Kirov, C. Capillas, J. Perez-Mato, and H. Wondratschek, *Acta Crystallographica Section A: Foundations of Crystallography* **62**, 115 (2006).
- [32] M. M. Seikh, V. Caignaert, V. Pralong, and B. Raveau, *J. Phys. Chem. Solids* **75**, 79 (2014).
- [33] M. Motin Seikh, T. Sarkar, V. Pralong, V. Caignaert, and B. Raveau, *J. Appl. Phys.* **113**, 053910 (2013).
- [34] Edited by H. Theo, IUCr, *International Tables for Crystallography, Volume A: Space Group Symmetry*, 5th ed., International Tables for Crystallography (Kluwer Academic Publishers, Dordrecht, Boston, London, 2002).
- [35] The transformation matrix between both settings is $(b, a, -c)$.
- [36] L. Pauling, H. P. Klug, and A. N. Winchell, *Am. Mineral.* **20**, 492 (1935).
- [37] L. C. Chapon, P. G. Radaelli, H. Zheng, and J. F. Mitchell, *Phys. Rev. B* **74**, 172401 (2006).
- [38] D. D. Khalyavin, P. Manuel, B. Ouladdiaf, A. Huq, P. W. Stephens, H. Zheng, J. F. Mitchell, and L. C. Chapon, *Phys. Rev. B* **83**, 094412 (2011).
- [39] L. Torre, G. Aurelio, E. Granado, and R. Sánchez, *J. Solid State Chem.* **230**, 34 (2015).
- [40] D. D. Khalyavin, L. C. Chapon, P. G. Radaelli, H. Zheng, and J. F. Mitchell, *Phys. Rev. B* **80**, 144107 (2009).
- [41] A. Huq, J. Mitchell, H. Zheng, L. Chapon, P. Radaelli, K. Knight, and P. Stephens, *J. Solid State Chem.* **179**, 1136 (2006).
- [42] S. N. Panja, J. Kumar, S. Dengre, and S. Nair, *J. Phys.: Condens. Matter* **28**, 486001 (2016).
- [43] M. Valldor, Y. Sanders, and W. Schweika, *J. Phys.: Conf. Ser.* **145**, 012076 (2009).
- [44] Jmol: an open-source Java viewer for chemical structures in 3D, <http://www.jmol.org/>.
- [45] T. Sarkar, M. M. Seikh, V. Pralong, V. Caignaert, and B. Raveau, *J. Mater. Chem.* **22**, 18043 (2012).
- [46] M. M. Seikh, V. Pralong, V. Caignaert, and B. Raveau, *Z. Anorganische Allgemeine Chem.* **640**, 1141 (2014).
- [47] N. Qureshi, M. T. Fernández Díaz, L. C. Chapon, A. Senyshyn, W. Schweika, and M. Valldor, *Phys. Rev. B* **97**, 064404 (2018).